# Effects of a random gauge field on the conductivity of graphene sheets with disordered ripples

Rhonald Burgos, Jesus Warnes, Leandro R. F. Lima, and Caio Lewenkopf*
*Instituto de Física, Universidade Federal Fluminense, 24210-346 Niterói RJ, Brazil*
(Received 14 November 2014; revised manuscript received 19 January 2015; published 2 March 2015)

We study the effect of disordered ripples on the conductivity of monolayer graphene flakes. We calculate the relaxation times and the Boltzmann conductivities associated with two mechanisms. First, we study the conductivity correction due to an external in-plane magnetic field $B_\parallel$. Due to the irregular local curvature found in graphene sheets deposited over a substrate, $B_\parallel$ can be mapped into an effective random magnetic field perpendicular to the graphene surface. Second, we study the electron momentum relaxation due to intrinsic pseudomagnetic fields originated from deformations and strain. We find that the competition between these mechanisms gives rise to a strong anisotropy in the conductivity tensor. This result provides a new strategy to quantitatively infer the strength of pseudomagnetic fields in rippled graphene flakes.

DOI: 10.1103/PhysRevB.91.115403 PACS number(s): 72.80.Vp, 73.23.−b, 72.10.−d

## I. INTRODUCTION

The electronic transport properties of bulk graphene are quite remarkable [1–4]. At room temperature graphene on $SiO_2$ substrates has mobilities [5] as high as $\mu \approx 15\,000\ \mathrm{cm^2\,V^{-1}\,s^{-1}}$, which are significantly larger than those of any other semiconductor. At low temperatures, however, the typical mobilities increase only up to $\mu \approx 200\,000\ \mathrm{cm^2\,V^{-1}\,s^{-1}}$, which is a disappointing figure compared with those of high-quality GaAs heterostructures. These observations triggered intense theoretical and experimental activity to understand the disorder mechanisms that limit the mobility in graphene (see, for instance, Refs. [1–4] for a review). The theoretical understanding, acquired from analysis of the Boltzmann equation [1,3], numerical simulations [2,6,7], and field theoretical techniques [8], is that extrinsic disorder such as ad-atoms absorbed in the graphene surface and substrate charge inhomogeneities and intrinsic disorder such as vacancies play a key role.

Motivated by recent experiments [9–12], we study the effect of extrinsic and intrinsic random gauge potential disorder due to strain. We show that, although unlikely to be dominant in graphene deposited over standard substrates, these kinds of disorder make unique and sizable contributions to the conductivity. For high-quality substrates, there is even experimental evidence [12] that random strain could be a good candidate for the leading electron relaxation mechanism in on-substrate graphene.

Standard electronic transport experiments use samples where graphene flakes are deposited over an insulating substrate. In this setting, it has been experimentally established that the graphene surface is characterized by disordered static ripples [13–16]. For $SiO_2$ substrates, the latter have typical lengths of $\lambda \approx 5 - 30$ nm and characteristic heights of $h_{\mathrm{rms}} \approx 0.2 - 0.5$ nm.

Lattice deformations due to ripples change the distance between the atoms in the graphene sheet. At the quantum level, site lattice displacements change the orbital bonding between the corresponding atoms, modifying the electronic structure of the material. In graphene, whose low-energy electronic properties are nicely described by a nearest-neighbor tight-binding model [1], the occurrence of ripples changes the tight-binding hopping terms [1,17,18]. For distortions with length scales much larger than the lattice parameter, characteristic of most samples [13–16], it has been shown that the tight-binding model can be mapped into an effective Dirac Hamiltonian with a pseudomagnetic vector potential [1,19–21] that depends on the lattice distortions. Hence, random ripples give rise to an *intrinsic* random gauge potential. The experimental evidence of pseudomagnetic fields is scarce and indirect but quite remarkable. Strain fields have been invoked to associate the local density of states observed in graphene nanobubbles [22] to Landau levels with energies corresponding to very high magnetic fields. To the best of our knowledge, no transport experiment has yet observed manifestations of this physical picture.

Random magnetic fields can also be achieved by realizing that disordered ripples in graphene and the roughness at semiconductor interface heterostructures share several common features. Starting in the late 1980s, a number of ingenious methods were used to characterize the interface roughness in heterostructures [23–25]. One idea is particularly suited for graphene studies: By applying a strong magnetic field $B_\parallel$, aligned with the plane of a heterostructure interface confining a two-dimensional electron gas (2DEG), the (smooth) interface roughness disorder gives origin to a local random magnetic field perpendicular to the 2DEG surface. Analysis of the electronic transport properties as a function of the applied magnetic field gives quantitative information about the interface roughness.

This setting was nicely explored in a recent experiment [9], which combined information on the average conductivity and its weak localization correction [26,27] in graphene to extract the sample characteristic $\lambda$ and $h_{\mathrm{rms}}$. This procedure has also been used in the experimental study of other graphene systems [10,11]. Theory [28] shows that an applied $B_\parallel$ on a rough surface gives rise to an effective dephasing $\ell_\phi$ and to suppression of the weak localization peak. In addition to this quantum correction, the random magnetic field due to $B_\parallel$ also contributes to the electron momentum relaxation, which at high doping is accounted for by the Boltzmann theory [9]. This nice analysis does not consider the effect of intrinsic pseudomagnetic fields due to strain, discussed above.

*caio@if.uff.br

 

Our focus is different. We study the combined effect of intrinsic and extrinsic random magnetic fields on the Drude conductivity. We revisit the analysis of the Boltzmann equation in graphene [1,2,4,29] and calculate the contributions of random magnetic fields to the Drude conductivity. We show that the conductivity corrections due to an applied in-plane magnetic field $B_\parallel$ on a rippled graphene flake depend on the direction of $B_\parallel$ and are very anisotropic. We find that this result can be reconciled with the experimental findings in Ref. [9] by theoretically treating the effect of strain and $B_\parallel$ on the same footing. We also show that the combined effect of both sources of random magnetic fields provides a new experimental path to quantitatively probe the effects of strain fields in the low-energy electronic dynamics of graphene.

The paper is structured as follows: In Sec. II we present the disorder model we employ to describe ripples and the corresponding effective Hamiltonian. We briefly explain the origin of an effective random field due to an applied in-plane magnetic field $B_\parallel$, as well as from the intrinsic strain field due to ripples. In Sec. III we calculate the contributions to the Drude conductivity due to $B_\parallel$ and strain using the Boltzmann transport equation. We show how to account for the disorder potential anisotropy and discuss its consequences comparing with experiments. Finally, in Sec. IV we present our conclusions and an outlook.

## II. MODEL HAMILTONIAN

In this section we present a model to study the effect of extrinsic and intrinsic sources of random magnetic fields in the dynamics of electrons in corrugated graphene monolayer samples. Close to the charge neutrality point, the electronic dispersion relation of pristine graphene monolayers is linear and has two degenerate components, with corresponding $K$ and $K'$ valley indices [1]. In the presence of a magnetic field, the effective electronic Hamiltonian for the $K$ valley reads

$$H^K = v_F \boldsymbol{\sigma}\cdot[\boldsymbol{p} + e\boldsymbol{A}(\boldsymbol{r})] = H_0^K + V(\boldsymbol{r}), \tag{1}$$

where the vector potential $\boldsymbol{A}(\boldsymbol{r})$ has been included in $H^K$ by minimal coupling. Here $v_F \approx 10^6$ m/s, $\boldsymbol{\sigma}$ are the Pauli matrices acting on the sublattice space, and $\boldsymbol{p}$ is the electron momentum operator. The Hamiltonian for the $K'$ valley has a similar structure [1].

In this description, a generic long-ranged disorder potential, $V(\boldsymbol{r})$, is represented in both $K$ and $K'$ valleys by

$$V(\boldsymbol{r}) = \sum_i \sigma_i V^{(i)}(\boldsymbol{r}), \tag{2}$$

where $i = 0$ stands for scalar disorder (with $\sigma_0 = I_2$) and $i = 1,2$ for vector potential disorder, while $i = 3$ represents a mass term. The focus of our study is (intrinsic and extrinsic) disordered gauge fields, associated with $V^{(1)}$ and $V^{(2)}$. In this paper we do not consider scalar disorder.

Let us introduce

$$\langle \boldsymbol{k}'s'|V|\boldsymbol{k}s\rangle = \tfrac{1}{2}[1 + ss'e^{i(\theta-\theta')}]V^{(0)}_{\boldsymbol{k}-\boldsymbol{k}'} + \frac{se^{i\theta}}{2}\left(V^{(1)}_{\boldsymbol{k}-\boldsymbol{k}'} - iV^{(2)}_{\boldsymbol{k}-\boldsymbol{k}'}\right) + \frac{s'e^{-i\theta'}}{2}\left(V^{(1)}_{\boldsymbol{k}-\boldsymbol{k}'} + iV^{(2)}_{\boldsymbol{k}-\boldsymbol{k}'}\right), \tag{3}$$

where the spinor

$$|\boldsymbol{k}s\rangle = \frac{1}{\sqrt{2\mathcal{A}}}\begin{pmatrix}1\\ se^{i\theta}\end{pmatrix}e^{i\boldsymbol{k}\cdot\boldsymbol{r}} \tag{4}$$

is an eigenstate of $H_0^K$, $\theta = \tan^{-1}(k_y/k_x)$, $s$ indicates particle ($s = +1$) or hole ($s = -1$) doping, and

$$V^{(i)}_{\boldsymbol{k}-\boldsymbol{k}'} = \frac{1}{\mathcal{A}}\int d\boldsymbol{r}\, e^{i(\boldsymbol{k}-\boldsymbol{k}')\cdot\boldsymbol{r}}\, V^{(i)}(\boldsymbol{r}) \tag{5}$$

is the momentum representation of $V^{(i)}$. Since we deal with elastic processes, in the remainder of the paper we assume that $s = s'$.

At low temperatures, scalar disorder (short and long ranged) is the main source of momentum relaxation in graphene systems [2,4]. In this paper we use a phenomenological transport time $\tau_s$ to account for effects of scalar disorder in the conductivity. We assume that $\tau_s$ is much shorter than the characteristic transport times due to random gauge fields. In Sec. IV, where we compare our results to experiments, we show that $\tau_s$ indeed dominates the conductivity in graphene, but some transport properties are only explained by including effects due to random gauge fields.

The ripple disorder model employed in this study is defined as follows: We describe the graphene sheet surface by $z = h(\boldsymbol{r})$, where $h$ is the surface displacement with respect to the reference plane $z = 0$ at the position $\boldsymbol{r} = (x,y)$. The average of $h$ is set to 0. In line with the experiments on graphene deposited over a substrate [9,13–16], we further assume that the typical heights $h_{\rm rms}$ are much smaller than the ripple lengths $\lambda$.

We model the ripple fluctuations in $h(\boldsymbol{r})$ by the correlation function

$$\langle h(\boldsymbol{r})h(\boldsymbol{r}')\rangle = h_{\rm rms}^2\, F\left(\frac{|\boldsymbol{r}-\boldsymbol{r}'|}{\lambda}\right), \tag{6}$$

where $\langle\cdots\rangle$ denotes the average over disorder. Although theory predicts a power-law height-height correlation function for free-standing membranes [30], experiments support single-parameter correlations for the (static) ripples of graphene deposited over a substrate. For later convenience, let us define

$$h(\boldsymbol{q}) = \frac{1}{\mathcal{A}}\int d\boldsymbol{r} e^{i\boldsymbol{q}\cdot\boldsymbol{r}}h(\boldsymbol{r}), \tag{7}$$

where $\mathcal{A}$ is the sample size. In reciprocal space,

$$\langle h(\boldsymbol{q})h(\boldsymbol{q}')\rangle = h_{\rm rms}^2\, \overline{F}(\boldsymbol{q})\delta_{\boldsymbol{q},-\boldsymbol{q}'}, \tag{8}$$

where $\overline{F}(\boldsymbol{q})$ is the Fourier transform of the correlation function $F(|\boldsymbol{r}-\boldsymbol{r}'|)$.

We address two mechanisms that generate random magnetic fields. First, we study the case of an external strong magnetic field $\boldsymbol{B}_\parallel$ applied parallel to the graphene sheet. We show that, due to the ripples, $\boldsymbol{B}_\parallel$ gives rise to a random effective magnetic field $B_{\rm ext}(\boldsymbol{r})$ perpendicular to the graphene surface. Next, we discuss the intrinsic pseudomagnetic field $\boldsymbol{B}_{\rm int}$ originating from the strain field corresponding to the graphene sheet profile height $h(\boldsymbol{r})$.

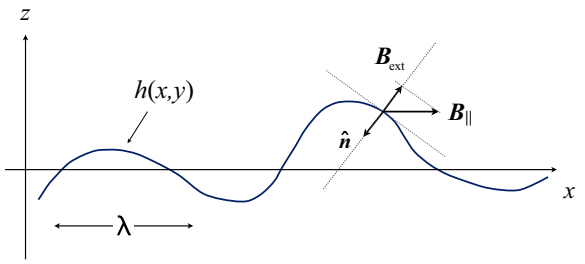


FIG. 1. (Color online) Sketch of $h(\boldsymbol{r})$ along the $x$ direction. Ripple amplitudes $\delta h$ are enhanced and made comparable with $\lambda$ to aid the illustration. For convenience, we take $\boldsymbol{B}_\parallel = B_\parallel \hat{\boldsymbol{x}}$.

### A. Random magnetic fields due to ripples and an in-plane external $B$ field

Let us first consider the setup of a magnetic field applied parallel to the sample, $z = 0$, which has been experimentally investigated in a variety of systems [9,23–25]. For notational convenience, in what follows we fix the direction of $B_\parallel$ along the $x$ axis; namely, $\boldsymbol{B}_\parallel = B_\parallel \hat{\boldsymbol{x}}$.

As illustrated in Fig. 1, the parallel magnetic field $\boldsymbol{B}_\parallel$ has a component perpendicular to the surface $z = h(\boldsymbol{r})$ that is given by

$$B_{\rm ext}(\boldsymbol{r}) = -\boldsymbol{B}_\parallel \cdot \hat{\boldsymbol{n}}(\boldsymbol{r}). \tag{9}$$

At the point $\boldsymbol{r}_0 = (x_0, y_0)$, the surface $z = h(\boldsymbol{r})$ has a unit normal vector,

$$\hat{\boldsymbol{n}}(\boldsymbol{r}_0) = \frac{1}{\sqrt{1 + \left(\frac{\partial h}{\partial x}\right)^2 + \left(\frac{\partial h}{\partial y}\right)^2}} \begin{pmatrix} \partial h/\partial x \\ \partial h/\partial y \\ -1 \end{pmatrix}\Bigg|_{\boldsymbol{r}=\boldsymbol{r}_0}. \tag{10}$$

We assume that the typical displacement magnitude is characterized by $\delta h$. For $\delta h \ll \lambda$, we write

$$\hat{\boldsymbol{n}}(\boldsymbol{r}_0) \approx (\partial h/\partial x, \partial h/\partial y, -1)|_{\boldsymbol{r}=\boldsymbol{r}_0}. \tag{11}$$

Hence, the effective local perpendicular magnetic field reads

$$B_{\rm ext}(\boldsymbol{r}) = -\boldsymbol{B}_\parallel \cdot \nabla h(\boldsymbol{r}) \tag{12}$$

and is expressed, in a convenient gauge for $\boldsymbol{B}_\parallel = B_\parallel \hat{\boldsymbol{x}}$, by the vector potential

$$A_x(\boldsymbol{r}) = 0 \quad \text{and} \quad A_y(\boldsymbol{r}) = -B_\parallel h(\boldsymbol{r}). \tag{13}$$

Figure 2(a) illustrates a typical disorder realization of $h(\boldsymbol{r})$ with fluctuations characterized by the Gaussian correlation function $F(x) = \exp(-x^2/2\lambda^2)$. The corresponding magnetic field $B_{\rm ext}(\boldsymbol{r})$, normal to the graphene sheet, is shown in Fig. 2(b). While $h(\boldsymbol{r})$ displays an isotropic disorder, $B_{\rm ext}(\boldsymbol{r})$ is clearly anisotropic. The anisotropy direction of $B_{\rm ext}(\boldsymbol{r})$ depends on the orientation of $B_\parallel$.

The anisotropy is quantified by inspecting the autocorrelation function

$$\langle B_{\rm ext}(\boldsymbol{r}) B_{\rm ext}(\boldsymbol{r}')\rangle = B_\parallel^2 \left\langle \frac{\partial h(\boldsymbol{r})}{\partial x} \frac{\partial h(\boldsymbol{r}')}{\partial x'} \right\rangle, \tag{14}$$

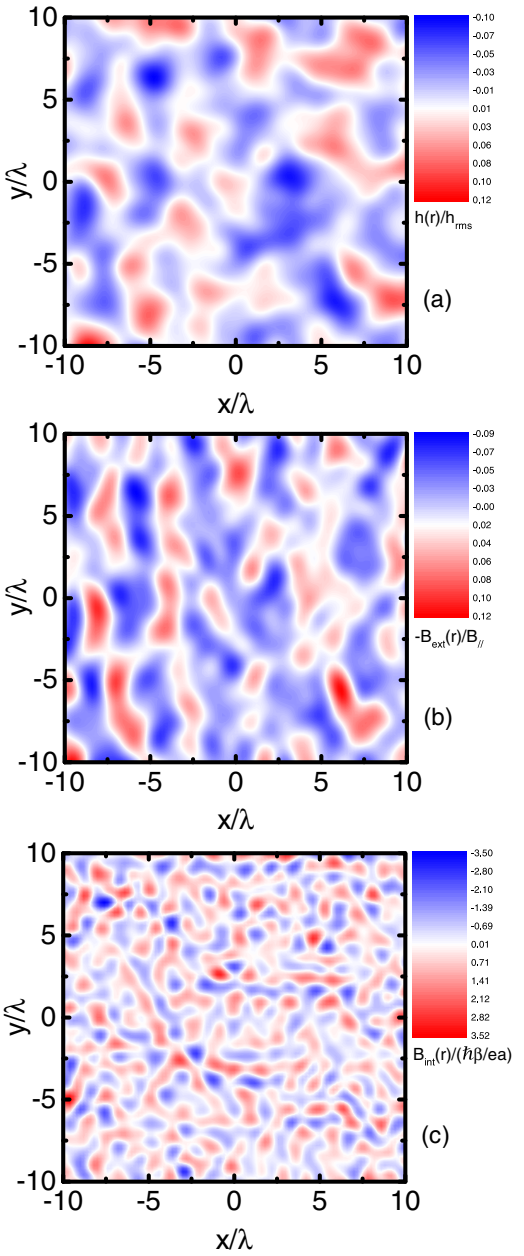


FIG. 2. (Color online) Typical disorder realization of (a) $h(\boldsymbol{r})$, characterized by a Gaussian correlation function $F$; (b) the corresponding $B_{\rm ext}(\boldsymbol{r})$ for an external $\boldsymbol{B}_\parallel$ applied along the $x$ direction, defined in Eq. (12); and (c) $B_{\rm int}(\boldsymbol{r})$ due to lattice deformations, given by Eq. (19).

which can be expressed in terms of $F$ by direct differentiation. Alternatively, going to reciprocal space, one writes

$$\left\langle \frac{\partial h(\boldsymbol{r})}{\partial x} \frac{\partial h(\boldsymbol{r}')}{\partial x'} \right\rangle = h_{\rm rms}^2 \sum_{\boldsymbol{q}} q_x^2 \overline{F}(\boldsymbol{q}) e^{-i\boldsymbol{q}\cdot(\boldsymbol{r}-\boldsymbol{r}')}$$
$$= -h_{\rm rms}^2 \frac{d^2}{dx^2} F(\boldsymbol{\rho}), \tag{15}$$

with $\boldsymbol{\rho} = \boldsymbol{r} - \boldsymbol{r}'$.

Let us calculate $\langle B_{\rm ext}(\boldsymbol{r}) B_{\rm ext}(\boldsymbol{r}')\rangle$ for the case where $h(\boldsymbol{r})$ is characterized by a Gaussian correlation function, the same as in

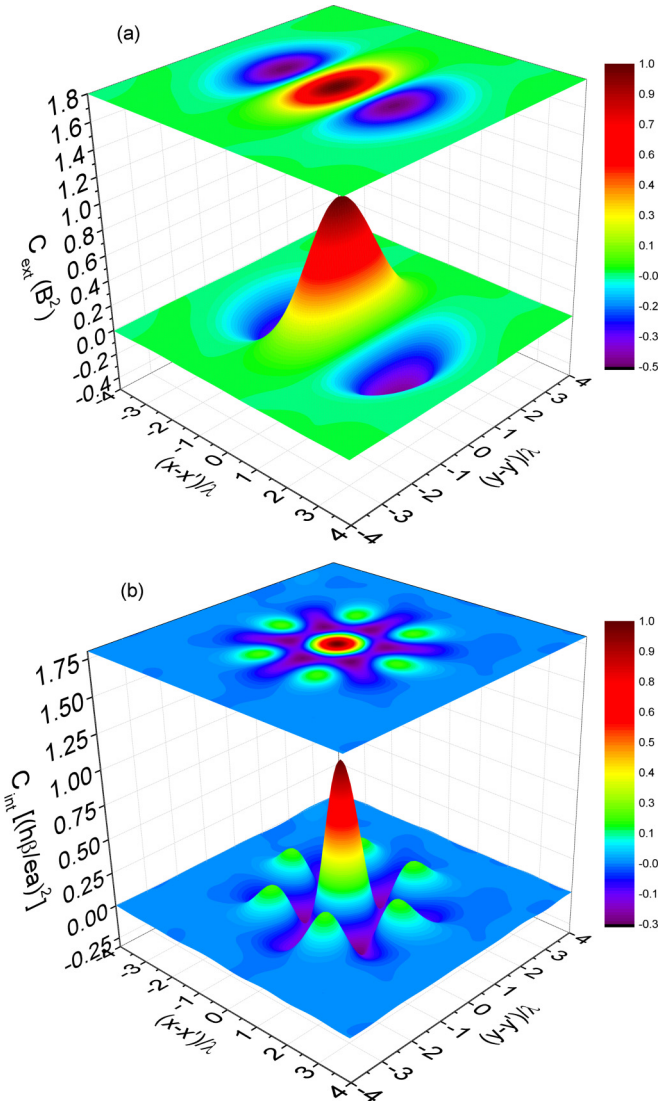


FIG. 3. (Color online) Extrinsic and intrinsic magnetic-field correlation functions: (a) $C_{\rm ext}(\boldsymbol{r}-\boldsymbol{r}')=\langle B_{\rm ext}(\boldsymbol{r})B_{\rm ext}(\boldsymbol{r}')\rangle$ for an external $\boldsymbol{B}_\parallel$ applied along the $x$ direction and (b) $C_{\rm int}(\boldsymbol{r}-\boldsymbol{r}')=\langle B_{\rm int}(\boldsymbol{r})B_{\rm int}(\boldsymbol{r}')\rangle$ due to strain, in units of $h_{\rm rms}^4/\lambda^6(\hbar\beta/ea)^2$, both corresponding to a ripple disordered surface $h(\mathbf{r})$ characterized by a Gaussian correlation function.

Fig. 2(a). The corresponding $B_{\rm ext}(\boldsymbol{r})$ autocorrelation function reads

$$\langle B_{\rm ext}(\boldsymbol{r})B_{\rm ext}(\boldsymbol{r}')\rangle = B_\parallel^2\frac{h_{\rm rms}^2}{\lambda^2}\left[1-\left(\frac{\rho}{\lambda}\right)^2\cos^2\alpha\right]e^{-\frac{\rho^2}{2\lambda^2}}, \quad (16)$$

where $\alpha$ is the angle between $\boldsymbol{B}_\parallel$ (or the $x$ axis) and $\boldsymbol{\rho}$.

Figure 3(a) shows the $B_{\rm ext}(\boldsymbol{r})$ autocorrelation function obtained by averaging over $10^5$ ripple disorder realizations of $h(\boldsymbol{r})$, as defined by Eq. (6) with a Gaussian correlation function $F$ (for more details see, for instance, Ref. [6]). As expected, it coincides with Eq. (16) and expresses the anisotropy captured by a visual inspection of Fig. 2(b).

### B. Pseudomagnetic fields due to strain

The out-of-plane deformations of a rippled membrane described by $h(\boldsymbol{r})$ can be associated with the strain tensor $u_{ij}(\boldsymbol{r})$ given by [19,31,32]

$$u_{xx}\approx\frac{1}{2}\left(\frac{\partial h}{\partial x}\right)^2,\quad u_{yy}\approx\frac{1}{2}\left(\frac{\partial h}{\partial y}\right)^2,\quad \text{and}$$
$$u_{xy}\approx\frac{1}{2}\left(\frac{\partial h}{\partial x}\frac{\partial h}{\partial y}\right). \quad (17)$$

For simplicity, we have neglected the effect of in-plane deformations.

The effect of strain on the low-energy electronic structure of graphene can be accounted for by introducing a scalar and a vector gauge potential in the Dirac equation [20,21,30]. The scalar term reads

$$V^{(0)}(\boldsymbol{r})=g[u_{xx}(\boldsymbol{r})+u_{yy}(\boldsymbol{r})], \quad (18)$$

while, for the $K$ valley and for an armchair crystallographic orientation along the $x$ axis, $\boldsymbol{A}=(A_x,A_y)$ is given by

$$A_x(\boldsymbol{r})=\frac{\hbar\beta\kappa}{ea}[u_{xx}(\boldsymbol{r})-u_{yy}(\boldsymbol{r})],$$
$$A_y(\boldsymbol{r})=-2\frac{\hbar\beta\kappa}{ea}u_{xy}(\boldsymbol{r}), \quad (19)$$

where $a=1.42$ Å is the bond length between nearest-neighboring carbon atoms, and $e$ is the electron charge. Here $g\approx 4$ eV, $\kappa\approx 1/3$, and $\beta=-\partial\log t/\partial\log a\approx 2$ are dimensionless material-dependent parameters [19,31] that characterize the coupling between the Dirac electrons and the lattice deformations, where $t\approx 3$ eV is the hopping integral between nearest-neighbor $\pi$ orbitals.

In summary, for any given $h(\boldsymbol{r})$ one can readily calculate the pseudomagnetic field $\boldsymbol{B}_{\rm int}=\nabla\times\boldsymbol{A}$. Since $A_z=0$ and neither $A_x$ nor $A_y$ depends on $z$, $\boldsymbol{B}_{\rm int}=B_{\rm int}\hat{\boldsymbol{z}}$. Figure 2(c) shows the $B_{\rm int}$ corresponding to the random rippled surface $h(\boldsymbol{r})$ in Fig. 2(a). Note that the typical correlation length of $B_{\rm int}(\boldsymbol{r})$ is much shorter than that of $h(\boldsymbol{r})$.

Let us calculate $\langle B_{\rm int}(\boldsymbol{r})B_{\rm int}(\boldsymbol{r}')\rangle$ for a random Gaussian-correlated $h(\boldsymbol{r})$, corresponding to Eq. (6) with $F(x)=e^{-x^2/2\lambda^2}$. To this end, we calculate the Fourier transform of the intrinsic pseudomagnetic field, namely,

$$B_{\rm int}(\boldsymbol{q})=i\frac{\hbar\beta\kappa}{ea}[q_y u_{xx}(\boldsymbol{q})+2q_x u_{xy}(\boldsymbol{q})-q_y u_{yy}(\boldsymbol{q})], \quad (20)$$

with

$$u_{ij}(\boldsymbol{q})=-\frac{1}{2}\sum_{\boldsymbol{q}'}q_i'(q_j-q_j')h(\boldsymbol{q}')h(\boldsymbol{q}-\boldsymbol{q}'), \quad (21)$$

where $i$ and $j$ label the Cartesian coordinates.

We use Eqs. (20) and (21) to write the correlation function of $B_{\rm int}$ in momentum space. The evaluation of $\langle B_{\rm int}(\boldsymbol{q})B_{\rm int}(-\boldsymbol{q})\rangle$ amounts to computing the corresponding $\langle u_{ij}(\boldsymbol{q})u_{i'j'}(-\boldsymbol{q})\rangle$, which results in four-$h$ correlation functions. This can be done exactly for Gaussian fluctuations and provides a good qualitative estimate for other cases [30].

We obtain

$$\langle B_{\rm int}(\boldsymbol{q})B_{\rm int}(-\boldsymbol{q})\rangle=\frac{h_{\rm rms}^4\pi}{32\lambda^2\mathcal{A}}\left(\frac{\hbar\beta\kappa}{ea}\right)^2q^2$$
$$\times[16+\lambda^4q^4\sin^2 3\theta]e^{-\lambda^2q^2/4}, \quad (22)$$

where $\theta$ is the angle between $\boldsymbol{q}$ and the $x$ direction. By Fourier transforming back to coordinate space, we arrive at

$$C_{\rm int}(\boldsymbol{r}-\boldsymbol{r}') \equiv \langle B_{\rm int}(\boldsymbol{r}) B_{\rm int}(\boldsymbol{r}')\rangle = \frac{h_{\rm rms}^4}{\lambda^6}\left(\frac{\hbar\beta\kappa}{ea}\right)^2 \times \left[8 - 20\frac{\rho^2}{\lambda^2} + 9\frac{\rho^4}{\lambda^4} - 2\frac{\rho^6}{\lambda^6}\sin^2 3\alpha\right] e^{-\rho^2/\lambda^2}, \tag{23}$$

where $\alpha$ is the angle between $\boldsymbol{\rho} = \boldsymbol{r} - \boldsymbol{r}'$ and the $x$ axis [33].

The correlation function $C_{\rm int}(\boldsymbol{r}-\boldsymbol{r}')$ has six symmetry axes, reflecting the underlying graphene honeycomb lattice symmetry [19]. In other words, information about the graphene crystal structure survives disorder averaging. Figure 3(b) shows $C_{\rm int}(\boldsymbol{r}-\boldsymbol{r}')$ obtained from $10^5$ numerical realizations of Gaussian-correlated disorder for $h(\boldsymbol{r})$. The numerical simulations serve as a helpful test to check our analytical results. As in the previous subsection, we verify excellent agreement within the statistical precision.

## III. DRUDE-BOLTZMANN CONDUCTIVITY

In this section we use the effective Dirac Hamiltonian, Eq. (1), to calculate the transport time and the Drude-Boltzmann conductivity of graphene monolayers in the presence of random gauge fields. High-mobility graphene samples have typical electronic mean free paths of $\ell \gtrsim 50$ nm. Recalling [1] that the carrier density is related to the Fermi wave number by $k_F = \sqrt{\pi|n|}$, one readily obtains that $k_F\ell \gg 1$ already for a doping where $|n| \approx 10^{11}$ cm$^{-2}$. This indicates that even for modest carrier densities a semiclassical transport description is justified. For $|n| \gtrsim 10^{11}$ cm$^{-2}$ the typical graphene conductivity in good samples is much larger than $e^2/h$, the order of magnitude of quantum contributions to the electronic transport, such as weak localization [2,26,27] and universal conductance fluctuations [34]. In such situations, the Boltzmann approach is very successful in assessing the conductivity, as shown by direct comparison with numerical simulations using an atomistic basis [6,35]. As one approaches the charge neutrality point, and $k_F\ell \lesssim 1$, the semiclassical method is no longer suited and one has to resort to more sophisticated approaches [2,8].

We now discuss how to add gauge field disorder in the Boltzmann approach. For long-ranged disorder, some authors [36–38] argue that it can be advantageous to include the disorder potential in the classical Liouvillian evolution, that is, to treat $V(\boldsymbol{r})$ on the *left-hand side* of the Boltzmann equation. This approach is justified in the "classical" regime, where $k_F\lambda \gg 1$, that is, where random fields with a characteristic length $\lambda$ vary slowly on the scale of $k_F^{-1}$. In typical graphene samples, where the ripple sizes $\lambda$ are of the order of a few to 10 nm [13–16], the latter inequality holds for a carrier density $|n| \gg 10^{12}$ cm$^{-2}$, which is much higher than the doping studied in most experiments [1].

In this study, we calculate transport times for both short- and long-ranged disorder by evaluating the corresponding Boltzmann collision integral (on the *right-hand side* of the equation). As mentioned in Sec. I, for graphene on standard substrates (the case of interest here), the random gauge field contribution to the conductivity is not the dominant one. Hence, the electron mean free path due to ripples is larger than $\ell$ and the arguments justifying the semiclassical approximation hold.

The Boltzmann equation for graphene under a uniform electric field $\boldsymbol{E}$ reads [1,39]

$$-e\boldsymbol{E}\cdot\frac{\partial\varepsilon_{\boldsymbol{k},s}}{\partial\boldsymbol{p}}\frac{\partial f_0}{\partial\varepsilon} = \sum_{\boldsymbol{k}',s'}(g_{\boldsymbol{k},s} - g_{\boldsymbol{k}',s'})\mathcal{W}_{\boldsymbol{k}',s\leftarrow\boldsymbol{k},s}, \tag{24}$$

where $\varepsilon_{\boldsymbol{k},s} = sv_F\hbar|\boldsymbol{k}|$, $f_0$ is the Fermi distribution function, $g_{\boldsymbol{k}} = f_{\boldsymbol{k}} - f_0$ is the deviation from equilibrium due to the electric field, and $W_{\boldsymbol{k}',s'\leftarrow\boldsymbol{k},s}$ is the transition rate from state $(\boldsymbol{k},s)$ to state $(\boldsymbol{k}',s)$, which we calculate using the Fermi golden rule, namely,

$$\mathcal{W}_{\boldsymbol{k}',s'\leftarrow\boldsymbol{k},s} = \frac{2\pi}{\hbar}\langle|\langle\boldsymbol{k}'s'|V|\boldsymbol{k}s\rangle|^2\rangle\delta(\varepsilon_{\boldsymbol{k},s} - \varepsilon_{\boldsymbol{k}',s'}), \tag{25}$$

where $V$ is a generic long-ranged disorder potential parametrized by Eq. (2). The $\delta$ function reflects the fact that we are dealing with elastic processes and, hence, $s = s'$. In our model, the transition rates do not depend on $s$. Accordingly we drop this index whenever its omission does not introduce an ambiguity.

The scattering processes we address are anisotropic. Calculation of the transport properties in this case is slightly different [40,41] from that in the standard isotropic case [39]. In this study, we adapt the nice method developed by Tokura [42]—which is briefly described in what follows—to calculate the transport times of massless Dirac electrons in graphene.

In both situations of interest, the scattering potential correlation functions have at least one symmetry axis. For convenience, we choose the $x$ axis along a symmetry axis and define [42]

$$g_{\boldsymbol{k}} = \left(-\frac{\partial f_0}{\partial\varepsilon_{\boldsymbol{k}}}\right)ev_{\boldsymbol{k}}\,\boldsymbol{\tau}(\theta)\cdot\boldsymbol{E}, \tag{26}$$

where $\boldsymbol{\tau}(\theta)$ is the relaxation time vector to be solved. We recall that $\theta$ is the angle between $\boldsymbol{k}$ and the $x$ axis. Note that $\boldsymbol{\tau}$ depends explicitly on $\theta$ and implicitly on $|\boldsymbol{k}|$.

The current density (spin and valley degeneracies included) is given by

$$\boldsymbol{j} = \frac{4}{\mathcal{A}}\sum_{\boldsymbol{k}} e\boldsymbol{v}_{\boldsymbol{k}}g_{\boldsymbol{k}} = \frac{e^2}{\pi^2}\int_0^\infty dkk\left(-\frac{\partial f_0}{\partial\varepsilon_{\boldsymbol{k}}}\right)\int_0^{2\pi}d\theta\, v_{\boldsymbol{k}}\,\boldsymbol{v}_{\boldsymbol{k}}[\boldsymbol{\tau}(\theta)\cdot\boldsymbol{E}], \tag{27}$$

from which one obtains the conductivity tensor

$$\sigma = \frac{e^2|\varepsilon_F|}{\hbar^2\pi^2}\int_0^{2\pi}d\theta\begin{pmatrix}\tau_x(\theta)\cos\theta & \tau_y(\theta)\cos\theta\\ \tau_x(\theta)\sin\theta & \tau_y(\theta)\sin\theta\end{pmatrix}, \tag{28}$$

where $\varepsilon_F$ is the Fermi energy, measured with respect to the charge neutrality point energy. For the sake of simplicity, in Eq. (28) we have taken the zero-temperature limit, namely, $-\partial f_0/\partial\varepsilon = \delta(\varepsilon - \varepsilon_F)$.

By substituting the ansatz, (26), in the Boltzmann equation, Eq. (24), one obtains an integral equation for $\boldsymbol{\tau}(\theta)$,

namely,

$$\cos\theta = \int_0^{2\pi} d\theta' [\tau_x(\theta) - \tau_x(\theta')] \mathcal{W}(\theta,\theta'), \tag{29}$$

$$\sin\theta = \int_0^{2\pi} d\theta' [\tau_y(\theta) - \tau_y(\theta')] \mathcal{W}(\theta,\theta'), \tag{30}$$

where $\theta'$ is the angle between $\boldsymbol{k}'$ and the $x$ axis, and

$$\begin{aligned}\mathcal{W}(\theta,\theta') &= \frac{\mathcal{A}}{(2\pi)^2}\int_0^\infty dk' k' \mathcal{W}_{\boldsymbol{k}',s\leftarrow\boldsymbol{k},s} \\ &= \frac{\mathcal{A}|\varepsilon_F|}{2\pi v_F^2 \hbar^3}\langle |\langle \boldsymbol{k}',s|V|\boldsymbol{k},s\rangle|^2\rangle,\end{aligned} \tag{31}$$

where, due to the zero-temperature limit, $k = k' = k_F$.

The matrix element $\langle \boldsymbol{k}',s|V|\boldsymbol{k},s\rangle$ depends on $\boldsymbol{q} = \boldsymbol{k} - \boldsymbol{k}'$ and $\varphi = \pi/2 + (\theta + \theta')/2$, the angle between $\boldsymbol{q}$ and the $x$ axis. Hence, $\mathcal{W}(\theta,\theta')$ is better cast as $\mathcal{W}(q_\zeta,\varphi)$. We use the standard notation $\zeta = |\theta - \theta'|$ and $q_\zeta = 2k_F \sin(\zeta/2)$.

By expressing $\tau_x$ and $\tau_y$ in terms of a Fourier series, one transforms Eqs. (29) and (30) into an (infinite) set of algebraic equations. Using the $x$-axis symmetry and that $\mathcal{W}(\theta,\theta') = \mathcal{W}(\theta',\theta)$ [43], one shows that [42]

$$\tau_x(\theta) = \sum_{n=1}^\infty \tau_x^{(n)} \cos[(2n-1)\theta], \tag{32}$$

$$\tau_y(\theta) = \sum_{n=1}^\infty \tau_y^{(n)} \sin[(2n-1)\theta]. \tag{33}$$

By inserting the above relations into Eq. (28), one concludes that the conductivity tensor is diagonal, with

$$\sigma_{xx} = \frac{e^2|\varepsilon_F|}{\hbar^2\pi}\tau_x^{(1)} \quad \text{and} \quad \sigma_{yy} = \frac{e^2|\varepsilon_F|}{\hbar^2\pi}\tau_y^{(1)}, \tag{34}$$

which supports the interpretation of $\boldsymbol{\tau}^{(1)}$ as a transport time vector.

The symmetry $\mathcal{W}(\theta,\theta') = \mathcal{W}(\theta',\theta)$ implies that $\mathcal{W}(q_\zeta,\varphi) = \mathcal{W}(q_\zeta,\varphi+\pi) = \mathcal{W}(q_\zeta,\varphi-\pi)$. In turn,

$$\mathcal{W}(q_\zeta,\varphi) = \sum_{n=0}^\infty \mathcal{W}_n(q_\zeta)\cos(2n\varphi), \tag{35}$$

with an obvious inversion relation.

By using the Fourier expansions for $\boldsymbol{\tau}(\theta)$ and $W(q_\zeta,\varphi)$, Eqs. (29) and (30) can be cast in matrix form [42],

$$\delta_{l,1} = \sum_{n=1}^\infty M^-_{l,n}\tau_x^{(n)} \quad \text{and} \quad \delta_{l,1} = \sum_{n=1}^\infty M^+_{l,n}\tau_y^{(n)}, \tag{36}$$

where the matrix elements of $M^\pm$ are [42]

$$M^\pm_{l,n} = \frac{(-1)^{l-n}}{2}[(1+\delta_{l,n})J_{|l-n|,n+l-1} \pm J_{n+l-1,|l-n|}], \tag{37}$$

with

$$J_{n,m} = \int_0^{2\pi} d\zeta\, \mathcal{W}_n(q_\zeta)[\cos(n\zeta) - \cos(m\zeta)]. \tag{38}$$

Finally, by inverting $M^\pm$ in Eq. (36), one writes the vector transport time components as

$$\tau_x^{(1)} = [(M^-)^{-1}]_{11} \quad \text{and} \quad \tau_y^{(1)} = [(M^+)^{-1}]_{11}. \tag{39}$$

Note that for isotropic scattering, all $\mathcal{W}_n$ with $n > 0$ are 0 and $M^\pm$ is diagonal, with elements $K_{l,l} = J_{0,2l-1}$. Hence, the vector transport time components coincide, $\tau_x^{(1)} = \tau_y^{(1)} = \tau^{(1)}$, and read

$$\frac{1}{\tau^{(1)}} = J_{0,1} = \int_0^{2\pi} d\zeta\, \mathcal{W}_0(q_\zeta)(1-\cos\zeta), \tag{40}$$

which is the standard expression for the transport time in isotropic systems.

### A. Effect of an in-plane magnetic field

Let us now calculate the effect of an external parallel magnetic field on the conductivity. From Eq. (13) we write the effective disorder potential for the $K$ valley as

$$V_{\text{ext}}(\boldsymbol{r}) = v_F e\sigma_y A_y(\boldsymbol{r}) = -v_F e B_\parallel h(\boldsymbol{r})\sigma_y. \tag{41}$$

We recall that $h(\boldsymbol{r})$ varies slowly in the scale of the lattice spacing, and hence, $V_{\text{ext}}(\boldsymbol{r})$ is long-ranged and does not mix valleys.

The momentum relaxation rate $W_{\boldsymbol{k}'\leftarrow\boldsymbol{k}}$ reads

$$\mathcal{W}_{\boldsymbol{k}'\leftarrow\boldsymbol{k}} = \delta(k-k')\frac{2\pi e^2 v_F}{\hbar^2}B_\parallel^2 \sin^2\left(\frac{\theta+\theta'}{2}\right)\frac{C_h(q)}{\mathcal{A}}, \tag{42}$$

where

$$C_h(q) = \int d\boldsymbol{r}\, e^{i\boldsymbol{q}\cdot\boldsymbol{r}}\,\langle h(0)h(\boldsymbol{r})\rangle \tag{43}$$

is the form factor of the height-height correlation function. Here $\langle\cdots\rangle$ indicates the disorder average.

From Eq. (31) we obtain

$$\mathcal{W}(q,\varphi) = \frac{(eB_\parallel)^2|\varepsilon_F|}{4\pi\hbar^3}C_h(q)(1+\cos 2\varphi), \tag{44}$$

which has only two nonzero Fourier components, namely,

$$\mathcal{W}_n(q) = \frac{(eB_\parallel)^2|\varepsilon_F|}{4\pi\hbar^3}C_h(q), \quad \text{for} \quad n = 0,1, \tag{45}$$

while $\mathcal{W}_n(q) = 0$ for $n \geqslant 2$. In this case, the $M^\pm$ matrix is tridiagonal and reads [42]

$$M^\pm = \begin{pmatrix} (1\mp\frac{1}{2})J_{0,1} & -\frac{1}{2}J_{1,2} & 0 & \cdots \\ -\frac{1}{2}J_{1,2} & J_{0,3} & -\frac{1}{2}J_{1,4} & \cdots \\ 0 & -\frac{1}{2}J_{1,4} & J_{0,5} & \cdots \\ \vdots & \vdots & \vdots & \ddots \end{pmatrix}. \tag{46}$$

The inverse transport time components are given by

$$\frac{1}{\tau_x^{(1)}} = \frac{3}{2}J_{0,1} - \Gamma_3 \quad \text{and} \quad \frac{1}{\tau_y^{(1)}} = \frac{1}{2}J_{0,1} - \Gamma_3, \tag{47}$$

where $\Gamma_3$ is isotropic and determined by the continued fraction relation

$$\Gamma_m = \frac{(J_{1,m-1})^2}{4(J_{0,m} - \Gamma_{m+2})}. \tag{48}$$

In practice, we compute $\Gamma_3$ by assuming that $\Gamma_{\overline{m}} = 0$ and subsequently iterating (48). The choice of $\overline{m}$ determines the precision of the calculation: The larger $\overline{m}$, the more accurate is $\Gamma_3$.

Assuming that $\Gamma_3 \ll J_{0,1}$ leads to an interesting result, that is,

$$\frac{1}{\tau_y^{(1)}} = \frac{1}{3\tau_x^{(1)}} = \frac{(eB_\parallel)^2|\varepsilon_F|}{8\pi\hbar^3}\int_0^{2\pi} d\zeta(1-\cos\zeta)C_h(q). \quad (49)$$

In this limit $\tau_y^{(1)}/\tau_x^{(1)} = 3$. In other words, for $\Gamma_3 \ll J_{0,1}$ the corrections to the conductivity due to $\boldsymbol{B}_\parallel$ lead to $\Delta\sigma_{yy} = 3\Delta\sigma_{xx}$, regardless of the dependence of the correlation function $C_h(q)$ on $q$.

For $\Gamma_3 = 0$ and $C_h(q) = 2\pi\lambda^2 h_{\rm rms}^2 e^{-\lambda^2 q^2/2}$, we write $\tau_{x,y}^{(1)}$ in closed analytical form, namely,

$$\frac{1}{\tau_y^{(1)}} = \frac{1}{3\tau_x^{(1)}} = \frac{(eB_\parallel)^2|\varepsilon_F|}{4\hbar^3}(\lambda h_{\rm rms})^2 \times e^{-\lambda^2 k_F^2}\left[I_0\left(\lambda^2 k_F^2\right) - I_1\left(\lambda^2 k_F^2\right)\right], \quad (50)$$

where $I_0$ and $I_1$ are modified Bessel functions of the first kind. We use $k_F = \sqrt{\pi|n|}$ [1] to express the conductivity in terms of the charge carrier density $n$. We conclude that the correction to the conductivity due to an in-plane magnetic field depends quadratically on $h_{\rm rms}B_\parallel$ and has a nontrivial dependence on $\lambda^2|n|$.

In the high-doping limit of $\lambda|n|^{1/2} \gg 1$, Eq. (50) gives the resistivity contribution of an in-plane magnetic field in a rippled graphene sheet,

$$\Delta\rho_{yy} = 3\Delta\rho_{xx} \approx \frac{1}{2\sqrt{2}\hbar}\frac{h_{\rm rms}^2}{\lambda}B_\parallel^2|n|^{-3/2}, \quad (51)$$

in agreement with Ref. [9].

Figure 4 shows the resistivity $\Delta\rho_{yy}$ versus the carrier density $n$ (due to particle-hole symmetry, we only show $n > 0$) for $\overline{m} = 3$ and $\overline{m} \to \infty$. The optimal $\overline{m}$ value to obtain convergence depends on $\lambda^2 n$. The inset shows $\Delta\rho_{yy}$ for $\lambda^2 n$ values outside the validity range of the asymptotic expansion. As discussed in the next section, the $\lambda^2 n$ range displayed in the inset corresponds to the typical experimental situation. We find that the $|n|^{-3/2}$ scaling predicted by the asymptotic expansion, (51), is only a rough approximation.

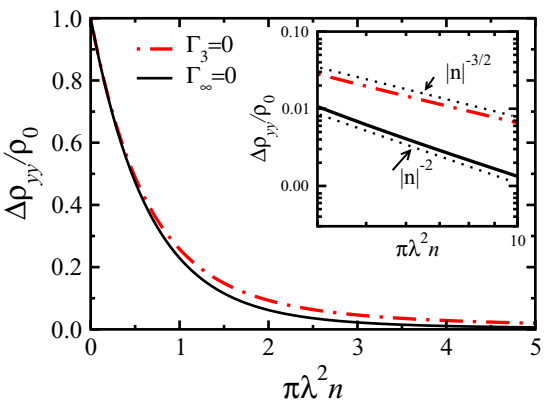


FIG. 4. (Color online) Resistivity $\Delta\rho_{yy}$, in units of $\rho_0 = (\pi\lambda h_{\rm rms}B_\parallel)^2/2\hbar$, due to $\boldsymbol{B}_\parallel$ as a function of $\lambda^2 n$. Inset: The same as the main plot, on a log-log scale to illustrate the dependence of $\Delta\rho_{xx}$ on $|n|$.

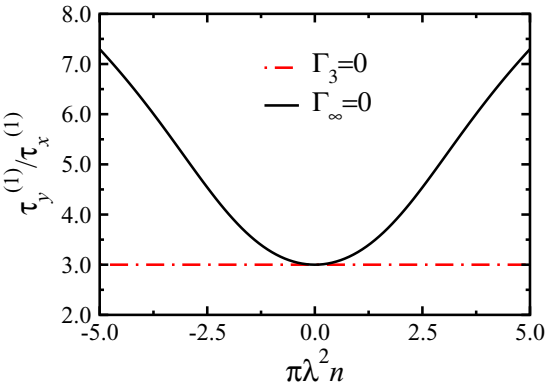


FIG. 5. (Color online) Ratio $\tau_y^{(1)}/\tau_x^{(1)}$ as a function of $\pi\lambda^2 n$. For $\pi\lambda^2 n < 5.0$, the limit $\overline{m} \to \infty$ is attained within an accuracy of $10^{-4}$ for $\overline{m} = 13$.

In general, $\Gamma_3$ is a nonvanishing correction to the transport time components, hence $\tau_y^{(1)}/\tau_x^{(1)} \neq 3$. However, for Gaussian ripple height correlations, the ratio $\tau_y^{(1)}/\tau_x^{(1)}$ is a function only of $\lambda k_F$.

Figure 5 shows $\tau_y^{(1)}/\tau_x^{(1)}$ versus $\lambda^2 n$. It illustrates the importance of $\Gamma_3$ in the calculation of the conductivity corrections. We find that with increasing carrier concentration, anisotropic conductivity is considerably favored.

The transport properties predicted by Eq. (50) are only slightly modified for the case of exponential ripple height correlations, $\langle h(0)h(\boldsymbol{r})\rangle = h_{\rm rms}^2 e^{-r/\lambda}$: For $\lambda|n|^{1/2} \gg 1$, the resistivity tensor given by Eq. (51) is multiplied [44] by a prefactor of the order of unity times $\log(\lambda^2|n|)$.

### B. Effect of strain fields

Let us now consider the effect of the pseudomagnetic fields due to strain, $B_{\rm int}$, in the conductivity of monolayer graphene sheets. In contrast to the mechanism discussed above, $B_{\rm int}(\boldsymbol{r})$ is solely determined by $h(\boldsymbol{r})$ and the material properties. Hence, it is intrinsic to any graphene sample with disordered ripples.

We use Eq. (19) to calculate the vector transport time $\boldsymbol{\tau}$ for the intrinsic effective vector potential due to strain. For the $K$ valley $V_{\rm int}$ reads

$$V_{\rm int}(\boldsymbol{r}) = \hbar v_F \frac{\beta\kappa}{a}\{[u_{xx}(\boldsymbol{r}) - u_{yy}(\boldsymbol{r})]\sigma_x - 2u_{xy}(\boldsymbol{r})\sigma_y\}. \quad (52)$$

In contrast with the previous subsection, here it is difficult to make quantitative progress without assuming a specific form for the ripple height correlation function. The qualitative behavior of the conductivity corrections due to strain that has been reported in the literature [30] is not sufficient for the analysis we propose.

As in Sec. II B, we calculate $\langle u_{ij}(\boldsymbol{r})u_{i'j'}(\boldsymbol{r}')\rangle$ by assuming Gaussian-correlated ripple height fluctuations, $C_h(q) = 2\pi\lambda^2 h_{\rm rms}^2 e^{-\lambda^2 q^2/2}$. After some lengthy but straightforward

algebra, we obtain

$$\langle|\langle \boldsymbol{k}'s|V_{\rm int}|\boldsymbol{k}s\rangle|^2\rangle = \frac{v_F^2\hbar^2\beta^2\kappa^2}{32a^2}\frac{\pi h_{\rm rms}^4}{\lambda^2\mathcal{A}} \times\left\{16+\lambda^4q^4\cos^2\left[\frac{3}{2}(\theta+\theta')\right]\right\}e^{-\lambda^2q^2/4}. \tag{53}$$

Using Eq. (31) we arrive at

$$\mathcal{W}(q,\varphi)=\mathcal{W}_{\rm int}\left[16+\frac{\lambda^4q^4}{2}(1+\cos 6\varphi)\right]e^{-\lambda^2q^2/4}, \tag{54}$$

where

$$\mathcal{W}_{\rm int}=\frac{\beta^2\kappa^2|\varepsilon_F|}{64a^2\hbar}\frac{h_{\rm rms}^4}{\lambda^2}. \tag{55}$$

(The notation is the same as that in the previous section.)

The only nonzero Fourier components of $\mathcal{W}(q,\varphi)$ are

$$\mathcal{W}_0(q)=\mathcal{W}_{\rm int}\left(16+\frac{\lambda^4q^4}{2}\right)e^{-\lambda^2q^2/4}\quad\text{and}$$
$$\mathcal{W}_3(q)=\mathcal{W}_{\rm int}\frac{\lambda^4q^4}{2}e^{-\lambda^2q^2/4}. \tag{56}$$

In this case, the $M^{\pm}$ matrix reads [42]

$$M^{\pm}=\begin{pmatrix} J_{0,1} & 0 & \mp\frac{1}{2}J_{3,2} & -\frac{1}{2}J_{3,4} & \cdots\\ 0 & J_{0,3}\mp\frac{1}{2}J_{3,0} & 0 & 0 & \cdots\\ \mp\frac{1}{2}J_{3,2} & 0 & J_{0,5} & 0 & \cdots\\ -\frac{1}{2}J_{3,4} & 0 & 0 & J_{0,7} & \cdots\\ \vdots & \vdots & \vdots & \vdots & \ddots \end{pmatrix}, \tag{57}$$

and the inverse transport time components are given by

$$\frac{1}{\tau_{x/y}^{(1)}}=J_{0,1}-\frac{(J_{3,2})^2}{4J_{0,5}}-\frac{(J_{3,4})^2}{4J_{0,7}}+\cdots. \tag{58}$$

Since $\tau_x^{(1)}=\tau_y^{(1)}$, the conductivity corrections due to the strain field are isotropic. This result seems to be at odds with the fact that the pseudomagnetic-field autocorrelation function $\langle B_{\rm int}(\boldsymbol{r})B_{\rm int}(\boldsymbol{r}')\rangle$ clearly shows a hexagonal symmetry, as illustrated in Fig. 3(b). As shown by Tokura [42], using general arguments, this is a false paradox: The conductivity tensor becomes anisotropic only for scattering processes characterized by a single symmetry axis, as in the $B_\parallel$ case, analyzed in the previous subsection.

Assuming that $J_{0,1}$ vastly dominates the sum in Eq. (58), we obtain

$$\frac{1}{\tau_{x/y}^{(1)}}=\mathcal{W}_{\rm int}\pi e^{-\lambda^2k_F^2/2}\left[\left(32+8\lambda^2k_F^2+16\lambda^4k_F^4\right)I_0\left(\lambda^2k_F^2/2\right) -\left(64+24\lambda^2k_F^2+16\lambda^4k_F^4\right)I_1\left(\lambda^2k_F^2/2\right)\right], \tag{59}$$

where $I_0$ and $I_1$ are modified Bessel functions of the first kind.

In the limit of $\lambda|n|^{-1}\gg 1$, we obtain the correction to the resistivity

$$\Delta\rho_{xx}=\Delta\rho_{yy}\approx\frac{h}{e^2}\frac{23\beta^2\kappa^2}{32\pi}\frac{h_{\rm rms}^4}{\lambda^2a^2}\lambda^{-3}|n|^{-3/2}. \tag{60}$$

The above asymptotic leading-order expansion for $\Delta\rho$ helps us to develop some insight into the relevant parameters. However, since the situation of $k_F\lambda\gg 1$ is hardly met in the current experimental situations of interest, it is necessary to numerically calculate the inverse transport times, as we do in the next subsection. As expected, the strain corrections to the conductivity depend on material parameters and are a nontrivial function of $\lambda$, $h_{\rm rms}$, and $|n|$. Since these corrections are small compared to other disorder effects, they are difficult to notice in standard transport experiments. This situation changes if we consider the combined effect of intrinsic and extrinsic random magnetic fields, as we discuss below.

### C. Combined effect of extrinsic and intrinsic random magnetic fields

We conclude this section by analyzing the combined effect of both previously discussed sources of random magnetic field disorder. As before, we assume that the system transport properties are dominated by other scattering processes, with a corresponding (isotropic) transport time $\tau_s$.

It is customary to use Matthiessen's rule when dealing with systems characterized by competing relaxation time mechanisms. In our case, Matthiessen's rule translates into adding the inverse transport times given by Eqs. (47) and (58), namely,

$$\frac{1}{\tau_{x/y}^{(1)}}=\frac{2\pm1}{2}J_{0,1}^{\rm ext}-\Gamma_3^{\rm ext}+J_{0,1}^{\rm int}-\frac{\left(J_{3,2}^{\rm int}\right)^2}{4J_{0,5}^{\rm int}}-\frac{\left(J_{3,4}^{\rm int}\right)^2}{4J_{0,7}^{\rm int}}+\cdots. \tag{61}$$

This naive approach was shown to be inaccurate when dealing with anisotropic potentials [42].

We analyze the combined effect of intrinsic and extrinsic random magnetic fields by considering an effective $M$ matrix given by

$$M_{\rm tot}^{\pm}=M_{\rm ext}^{\pm}+M_{\rm int}^{\pm}, \tag{62}$$

where $M_{\rm ext}^{\pm}$ and $M_{\rm int}^{\pm}$ are given by Eqs. (46) and (57), respectively. The $\boldsymbol{\tau}$ components are

$$\tau_x^{(1)}=[(M_{\rm tot}^{-})^{-1}]_{11}\quad\text{and}\quad\tau_y^{(1)}=[(M_{\rm tot}^{+})^{-1}]_{11}, \tag{63}$$

which, for $\overline{m}=5$, explicitly read

$$\frac{1}{\tau_{x/y}^{(1)}}=\left(1\pm\frac{1}{2}\right)J_{0,1}^{\rm ext}+J_{0,1}^{\rm int} +\frac{1}{\left(J_{0,3}^{\rm ext}+J_{0,3}^{\rm int}\mp J_{3,0}^{\rm int}big/2\right)\left(J_{0,5}^{\rm ext}+J_{0,5}^{\rm int}\right)-\left(J_{1,4}^{\rm ext}\right)^2/4} \times\left[-\frac{1}{4}\left(J_{0,5}^{\rm ext}+J_{0,5}^{\rm int}\right)\left(J_{1,2}^{\rm ext}\right)^2\mp\frac{1}{4}J_{3,2}^{\rm int}J_{1,2}^{\rm ext}J_{1,4}^{\rm ext} -\frac{1}{4}\left(J_{3,2}^{\rm int}\right)^2\left(J_{0,3}^{\rm ext}+J_{0,3}^{\rm int}\mp\frac{1}{2}J_{3,0}^{\rm int}\right)\right]+\cdots. \tag{64}$$

This result is clearly different from Eq. (61), since it mixes intrinsic and extrinsic effects. Let us now discuss the dependence of $\boldsymbol{\tau}$ on $B_\parallel$, $\lambda$, $h_{\rm rms}$, and $n$. For this purpose we numerically invert the matrix $M_{\rm tot}^{\pm}$, at order $\overline{m}\approx 30-50$ to guarantee an accuracy of $10^{-5}$ for the analyzed parameter range.

The resistivity corrections obtained from Matthiessen's rule, Eq. (61), depend quadratically on $B_\parallel$, in line with the

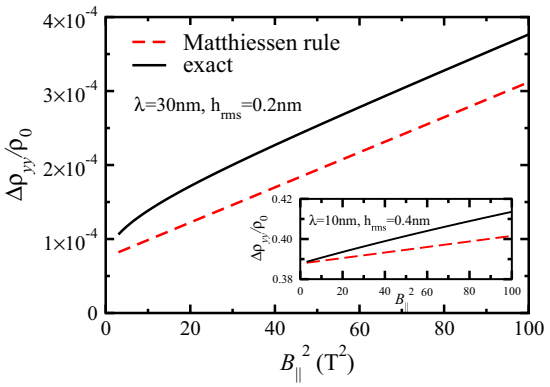


FIG. 6. (Color online) Resistivity correction $\Delta\rho_{yy}$, in units of $\rho_0 = (\pi\lambda h_{\rm rms} B_\parallel)^2/2\hbar$, as a function of the in-plane magnetic field $B_\parallel$ for $h_{\rm rms} = 0.2$ nm, $\lambda = 30$ nm, and $n = 10^{12}$ cm$^{-2}$. Inset: The same as the main figure, for $h_{\rm rms} = 0.4$ nm and $\lambda = 10$ nm.

experiment [9]. The full $M$-matrix analysis does not guarantee this simple dependence. In Fig. 6 we plot the resistivity correction $\Delta\rho_{yy}$ calculated using the full $M$ matrix and compare it with the one obtained from the Matthiessen rule, given by Eq. (61), for realistic values of $h_{\rm rms}$, $\lambda$, and $n$. The full $M$-matrix calculation (indicated as "exact") shows an overall higher resistivity than that obtained from the Matthiessen rule. It depends linearly on $B_\parallel^2$ for large $B_\parallel$ and deviates from this dependence only when $B_\parallel$ becomes small.

In contrast, the dependence of $\Delta\rho$ on $h_{\rm rms}$, $\lambda$, and $|n|$ is not trivial. For $h_{\rm rms}$ and $\lambda$ values taken close to those reported in topography experiments [13–16], a numerical study using the full $M$-matrix approach gives $\Delta\rho_{yy} \propto \lambda^{-\alpha}$ with $\alpha \approx 3\ldots4$, $\Delta\rho_{yy} \propto h_{\rm rms}^{\beta}$ with $\beta \approx 3$, and $\Delta\rho_{yy} \propto |n|^{-\gamma}$ with $\gamma \approx 2$. In summary, $\Delta\rho$ is very sensitive to small variations of $h_{\rm rms}$ and $\lambda$.

In Fig. 7 we compare Eqs. (47), (61), and (64) to gain insight into how the strain mechanism affects the ratio $\tau_y^{(1)}/\tau_x^{(1)}$. We find that the strain fields contribute to a strong suppression

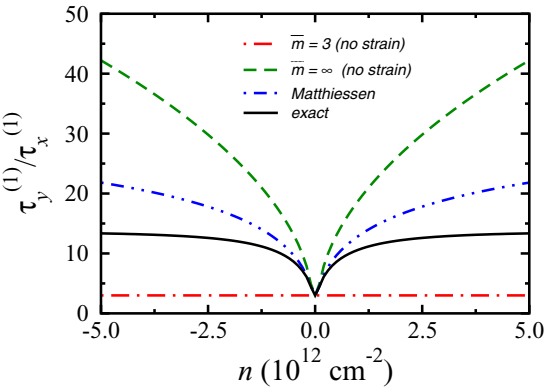


FIG. 7. (Color online) Anisotropy $\tau_y^{(1)}/\tau_x^{(1)}$ as a function of the carrier concentration $n$ using different approximation schemes, for $h_{\rm rms} = 0.2$ nm, $\lambda = 30$ nm, and $B_\parallel = 8$ T. The bottom, horizontal (red) line and the top (green) line stand for the contribution of $B_\parallel$ without accounting for strain fields. The second-from-the-top (blue) line represents the contributions of both external and strain fields using the conventional Matthiessen's rule. The black line shows the combined effect of intrinsic and extrinsic fields obtained for the full $M$-matrix analysis.

of the anisotropy in the transport time due to a strong $B_\parallel$. However, for realistic parameter values the anisotropy is still very large and of the order of $\tau_y^{(1)}/\tau_x^{(1)} \approx 10$ for $|n| \approx 10^{12}$ cm$^{-2}$.

In order to further compare our results with the experiment [9], let us introduce the magnetoresistance $\Delta\rho = \boldsymbol{E}\cdot\boldsymbol{j}/j^2$, where $j_x = j\cos\xi$, $j_y = j\sin\xi$, and $\xi$ is the angle between $\boldsymbol{B}_\parallel$ and $\boldsymbol{j}$. Using the relation $E_i = \rho_{ij} J_j$ one writes [45]

$$\Delta\rho(\xi) = \Delta\rho_{xx}\cos^2\xi + \Delta\rho_{yy}\sin^2\xi. \tag{65}$$

Reference [9] reports $\Delta\rho(70^{\rm o})/\Delta\rho(20^{\rm o}) \approx 0.13 - 0.26$. Using $\lambda$ and $h_{\rm rms}$ values obtained from atomic force microscopy (AFM) measurements, we obtain $\tau_y^{(1)}/\tau_x^{(1)} \approx 10$ for $n = 10^{12}$ cm$^{-2}$. This ratio leads to $\Delta\rho(70^{\rm o})/\Delta\rho(20^{\rm o}) \approx 0.2$, in good agreement with the experiment [9].

## IV. CONCLUSIONS AND OUTLOOK

In this paper we have studied the effect of random magnetic fields on the transport properties of a rippled graphene flake. We have used the Boltzmann equation, adapted to the case of anisotropic disorder [42], to address the case of an external magnetic field applied in-plane, the effect of intrinsic strain fields caused by graphene corrugation, and the combination of both.

We find that an external in-plane magnetic field $B_\parallel$ gives rise to very anisotropic conductivity corrections. By neglecting the effect of strain fields and using a parametrization of the ripple disorder that is consistent with experiments, we find conductivity corrections that scale with $B_\parallel^2$ and $|n|^{-2}$, consistent with Ref. [9]. In contrast, we obtain $\tau_y^{(1)}/\tau_x^{(1)}$ ratios as large as $20\ldots30$.

In the absence of an external magnetic field, random gauge fields due to ripple disorder make an *isotropic* contribution to the electron momentum relaxation in graphene, in line with the order of magnitude estimate presented in Ref. [30]. We find, however, that ripple disorder cannot be neglected in the analysis of the conductivity in the presence of a large $B_\parallel$. We also conclude that, due to the anisotropic nature of the problem, Matthiessen's rule is not accurate to address both intrinsic and extrinsic random fields on the same footing. For this purpose we have to invert the total $M$ matrix.

This approach allows us to successfully describe the corrections to the Drude conductivity reported in the experiment [9] using typical $\lambda$ and $h_{\rm rms}$ parameters taken from the AFM literature. In addition, we obtain a suppression of the resistivity anisotropy (with respect to the case where strain is neglected) that is consistent with Ref. [9]. We believe that the anisotropic nature of the random magnetic-field disorder also significantly changes the quantum corrections to the conductivity with respect to the isotropic result [28] and deserves further investigation.

In summary, our results suggest that the investigation of anisotropy corrections to the Drude conductivity could be a new and insightful path to experimentally quantify the effects of random pseudomagnetic fields due to strain.

**ACKNOWLEDGMENTS**

We thank Eduardo Mucciolo for numerous discussions. This work was supported by the INCT-Nanomateriais de Carbono and the Brazilian funding agencies: CAPES, CNPq, and FAPERJ.

[1] A. H. Castro Neto, F. Guinea, N. M. R. Peres, K. S. Novoselov, and A. K. Geim, Rev. Mod. Phys. **81**, 109 (2009).
[2] E. R. Mucciolo and C. H. Lewenkopf, J. Phys. Condens. Matter **22**, 273201 (2010).
[3] N. M. R. Peres, Rev. Mod. Phys. **82**, 2673 (2010).
[4] S. Das Sarma, S. Adam, E. H. Hwang, and E. Rossi, Rev. Mod. Phys. **83**, 407 (2011).
[5] A. K. Geim and K. S. Novoselov, Nat. Mater. **6**, 183 (2007).
[6] C. H. Lewenkopf, E. R. Mucciolo, and A. H. Castro Neto, Phys. Rev. B **77**, 081410(R) (2008).
[7] C. H. Lewenkopf and E. R. Mucciolo, J. Comput. Electron. **12**, 203 (2013).
[8] P. M. Ostrovsky, I. V. Gornyi, and A. D. Mirlin, Phys. Rev. B **74**, 235443 (2006).
[9] M. B. Lundeberg and J. A. Folk, Phys. Rev. Lett. **105**, 146804 (2010).
[10] S. Wada, N. Okuda, and J. Wakabayashi, Phys. E **42**, 1138 (2010).
[11] J. Wakabayashi and K. Sano, J. Phys. Soc. Jpn. **81**, 13702 (2012).
[12] N. J. G. Couto, D. Costanzo, S. Engels, D.-K. Ki, K. Watanabe, T. Taniguchi, C. Stampfer, F. Guinea, and A. F. Morpurgo, Phys. Rev. X **4**, 041019 (2014).
[13] M. Ishigami, J. H. Chen, W. G. Cullen, M. S. Fuhrer, and E. D. Williams, Nano Lett. **7**, 1643 (2007).
[14] V. Geringer, M. Liebmann, T. Echtermeyer, S. Runte, M. Schmidt, R. Rückamp, M. C. Lemme, and M. Morgenstern, Phys. Rev. Lett. **102**, 076102 (2009).
[15] A. Deshpande, W. Bao, F. Miao, C. N. Lau, and B. J. LeRoy, Phys. Rev. B **79**, 205411 (2009).
[16] W. G. Cullen, M. Yamamoto, K. M. Burson, J. H. Chen, C. Jang, L. Li, M. S. Fuhrer, and E. D. Williams, Phys. Rev. Lett. **105**, 215504 (2010).
[17] E.-A. Kim and A. H. Castro Neto, Europhys. Lett. **84**, 57007 (2008).
[18] F. de Juan, M. Sturla, and M. A. H. Vozmediano, Phys. Rev. Lett. **108**, 227205 (2012).
[19] F. Guinea, B. Horovitz, and P. Le Doussal, Phys. Rev. B **77**, 205421 (2008).
[20] A. Cortijo, F. Guinea, and M. A. H. Vozmediano, J. Phys. A **45**, 383001 (2012).
[21] M. A. H. Vozmediano, M. I. Katsnelson, and F. Guinea, Phys. Rep. **496**, 109 (2010).
[22] N. Levy, S. A. Burke, K. L. Meaker, M. Panlasigui, A. Zettl, F. Guinea, A. H. Castro Neto, and M. F. Crommie, Science **329**, 544 (2010).
[23] P. M. Mensz and R. G. Wheeler, Phys. Rev. B **35**, 2844 (1987).
[24] W. R. Anderson, D. R. Lombardi, R. G. Wheeler, and T.-P. Ma, IEEE Electron Device Lett. **14**, 351 (1993).
[25] D. M. Zumbühl, J. B. Miller, C. M. Marcus, V. I. Fal'ko, T. Jungwirth, and J. S. Harris Jr., Phys. Rev. B **69**, 121305 (2004).
[26] E. McCann, K. Kechedzhi, V. I. Fal'ko, H. Suzuura, T. Ando, and B. L. Altshuler, Phys. Rev. Lett. **97**, 146805 (2006).
[27] K. Kechedzhi, E. McCann, V. I. Fal'ko, H. Suzuura, T. Ando, and B. L. Altshuler, Eur. Phys. J. Spec. Top. **148**, 39 (2007).
[28] H. Mathur and H. U. Baranger, Phys. Rev. B **64**, 235325 (2001).
[29] D. S. Novikov, Appl. Phys. Lett. **91**, 102102 (2007).
[30] M. I. Katsnelson and A. K. Geim, Philos. Trans. R. Soc. A **366**, 195 (2008).
[31] H. Suzuura and T. Ando, Phys. Rev. B **65**, 235412 (2002).
[32] J. L. Mañes, Phys. Rev. B **76**, 045430 (2007).
[33] Since we only considered the out-of-plane contribution in the strain tensor, Eq. (22) gives a correlation function slightly different from the one found in Ref. [19], where a more general expression for the strain tensor was used.
[34] A. P. Hinz, S. Kettemann, and E. R. Mucciolo, Phys. Rev. B **89**, 075411 (2014).
[35] J. W. Kłos and I. V. Zozoulenko, Phys. Rev. B **82**, 081414 (2010).
[36] C. Kittel, *Quantum Theory of Solids*, 2nd ed. (Wiley, New York, 1987).
[37] P. Hedegard and A. Smith, Phys. Rev. B **51**, 10869 (1995).
[38] R. R. Brandão and L. Moriconi, arXiv:1410.6706.
[39] J. M. Ziman, *Principles of the Theory of Solids* (Cambridge University Press, Cambridge, 1972).
[40] C. Herring and E. Vogt, Phys. Rev. **101**, 944 (1956).
[41] E. H. Sondheimer, Proc. R. Soc. London A **268**, 100 (1962).
[42] Y. Tokura, Phys. Rev. B **58**, 7151 (1998).
[43] Microreversibility is usually invoked to guarantee $\mathcal{W}(\theta,\theta') = \mathcal{W}(\theta',\theta)$ and Eq. (24). In the presence of an external magnetic field, which breaks time-reversal symmetry, $\mathcal{W}(\theta,\theta') = \mathcal{W}(\theta',\theta)$ is still true within the approximation used in Eq. (25) .
[44] K. Genma and M. Katori, arXiv:1211.2046.
[45] A. W. Rushforth, B. L. Gallagher, P. C. Main, A. C. Neumann, M. Henini, C. H. Marrows, and B. J. Hickey, Phys. Rev. B **70**, 193313 (2004).